

Evidence for itinerant electron-local moment interaction in Li-doped α -MnTe

Tingjun Zhang,^{1,2,†} Steven J. Gomez Alvarado,^{1,2,†} Sijie Xu,^{1,2} Travis J. Williams,³ Xiaoping Wang,⁴ Junhong He,⁴ Matthew B. Stone,⁴ Colin Sarkis,⁴ Feng Ye,⁴ Zhaoyu Liu,^{1,2} Jinyulin Li,⁵ Aparna Jayakumar,^{1,2} Zehao Wang,^{1,2} Yaofeng Xie,^{1,2} Ching-Wu Chu,⁵ Liangzi Deng,⁵ Emilia Morosan,^{1,2} and Pengcheng Dai^{1,2,*}

¹*Department of Physics and Astronomy, Rice University, Houston, Texas 77005, USA*

²*Rice Laboratory for Emergent Magnetic Materials and Smalley-Curl Institute, Rice University, Houston, Texas 77005, USA*

³*ISIS Neutron and Muon Source, STFC Rutherford Appleton Laboratory, Didcot, Oxfordshire, OX11 0QX, United Kingdom*

⁴*Neutron Scattering Division, Oak Ridge National Laboratory, Oak Ridge, Tennessee 37831, USA*

⁵*Department of Physics and Texas Center for Superconductivity at the University of Houston, Houston, Texas 77204, USA*

We use inelastic neutron scattering to study the impact of Li doping on the semiconducting altermagnet α -MnTe. Introducing Li results in a spin reorientation from in-plane to out-of-plane and increases the density of itinerant carriers. While the spin waves in Li-doped α -MnTe remain largely Heisenberg-like, there is significant spin wave broadening across the entire Brillouin zone, signaling enhanced magnon damping induced by itinerant carriers. By extracting the local dynamic susceptibility and applying the total moment sum rule, we find that both undoped and Li-doped α -MnTe exhibit the full expected Mn^{2+} local moment of $\approx 5.9 \mu_B$ with $S = 5/2$. These results demonstrate that Li-doped α -MnTe hosts robust local-moment magnetism whose interactions are mediated via Ruderman-Kittel-Kasuya-Yosida-type interactions, highlighting the importance of itinerant carriers in magneto-transport and spin dynamic properties of altermagnets.

In conventional local-moment ferromagnets and antiferromagnets with dipolar magnetic exchange interactions, the collective motion of localized moments in the magnetic ordered state is spin waves (magnons) characterized by linear spin wave theories (LSWT) that ignore all terms of order higher than quadratic [1–4]. Since magnon-magnon interactions are negligible [5], the lifetime of magnons as measured by the energy width of spin wave spectra should be infinite and only limited by the instrumental resolution, as seen in ferromagnetic EuO [6] and collinear antiferromagnetic Rb_2MnF_4 [7]. The dispersion of spin waves determines the nearest-neighbor (NN), next-nearest-neighbor (NNN), etc. magnetic exchange couplings, and, therefore, the magnetic ordering temperature, regardless of the ordered moment direction controlled by the spin-orbit coupling (SOC) [4]. For classical spin systems (*i.e.*, $S \gg 1/2$) without strong quantum fluctuations, geometric frustration, or appreciable spin-lattice coupling, magnon decay processes are generally not expected in insulating magnets [5].

In metallic magnets, spin wave broadening can arise from a variety of interactions with conduction electrons. In itinerant systems, magnons can enter the Stoner particle-hole continuum at high energies, where they experience strong Landau damping [8–11]. In local-moment metals, low-energy spin-flip scattering of conduction electrons can produce Korringa-type damping in the long-wavelength limit. The phenomenological Landau-Lifshitz-Gilbert (LLG) model [12, 13] captures these long-wavelength relaxation processes, but these typically yield an extremely small intrinsic contribution to damping in three-dimensional bulk magnets. Even in the canonical metallic ferromagnet α -Fe, spin waves remain resolution-limited up to energies of order 200 meV, only

broadening upon entering the Stoner continuum [14–16]. Thus, significant spin wave damping is often weak or difficult to observe, and in systems with mixed local moment / itinerant character, its magnitude can depend sensitively on the structure of the Fermi surface.

In the semiconducting altermagnet α -MnTe, the opposite magnetic sublattices of Mn^{2+} are connected by symmetry operations that are not inversion (\mathcal{P}) or translation (t) symmetric due to the specific local crystal environment [Fig. 1(a)]. This leads to alternating spin splitting of electronic energy bands, arising from exchange coupling rather than SOC [17–19]. This is in sharp contrast to most collinear antiferromagnets, where the combination of time-reversal symmetry (\mathcal{T}) and \mathcal{P} or t symmetries between opposite magnetic sublattices enforces the degeneracy of electronic bands throughout the entire Brillouin zone (BZ) in the limit of zero SOC [4]. Indeed, several phenomena commonly associated with the breaking of \mathcal{T} -symmetry – spin-split electronic bands [20], anomalous Hall effects (AHE) [21–25], and magnetic circular dichroism [26] – have been experimentally realized in altermagnetic materials [27, 28]. In addition to momentum-dependent electronic energy band splitting, altermagnetic symmetry also gives rise to a momentum-dependent energy splitting of chiral magnons which is non-relativistic in origin and holds even in the limit of symmetric exchange interactions [29].

An attractive aspect of α -MnTe in the context of spintronics is the tunability of its altermagnetic ground state, which can be modified by chemical substitution [30, 31], uniaxial strain [23–25], and external applied fields [32–36]. α -MnTe adopts a layered *A*-type magnetic order below $T_{\text{AM}} = 307$ K [37–41], where Mn^{2+} moments are oriented along the NNN Mn-Mn direction [Fig. 1(a,b)]

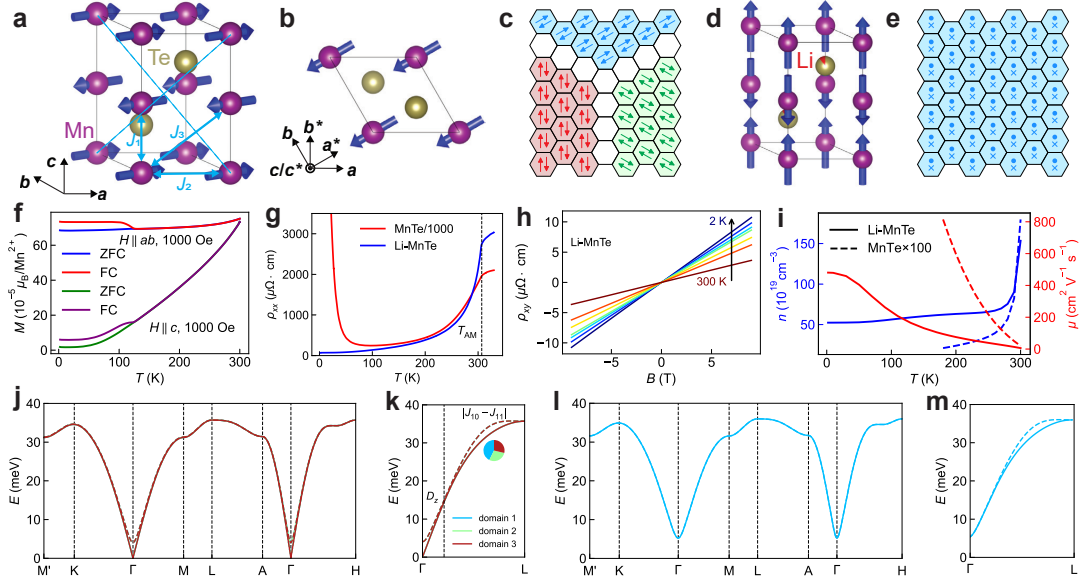


FIG. 1. (a,b) Parallel and top views of the lattice and magnetic structures of α -MnTe, highlighting magnetic moment directions and exchange couplings. The dashed lines indicate the altermagnetic exchange interactions J_{10} and J_{11} . (c,e) Schematics of magnetic domain configurations in undoped and Li-doped α -MnTe, respectively. The edges of the hexagons are parallel to \mathbf{a} and equivalent crystallographic directions in panel (b). (d) Parallel view of the lattice and magnetic structures of Li-doped α -MnTe, illustrating Li atoms (occupancy exaggerated) occupying Te-site defects. (f) Magnetization M of Li-doped α -MnTe versus temperature T . (g) Longitudinal resistivity ρ_{xx} versus temperature T for undoped and Li-doped α -MnTe. (h) Transverse resistivity ρ_{xy} of Li-doped α -MnTe. (i) Carrier density n and mobility μ of undoped and Li-doped α -MnTe. (j,k) Calculated spin waves of undoped α -MnTe for three domains within (j) and outside (k) the nodal planes. The calculations use exchange parameters from Ref. [29]. The inset in (k) displays the intensity contributions from the three domains at the point of altermagnetic splitting. The solid and dashed lines denote different branches of the spin waves, and the vertical dashed line separates the splitting dominated by single-ion anisotropy (D_z) and altermagnetism ($|J_{10} - J_{11}|$). (l,m) Calculated spin waves of Li-doped α -MnTe, with the single-ion anisotropy replaced by the value reported in Ref. [30].

[24]. The hexagonal in-plane symmetry enforces the coexistence of three degenerate magnetic domains, each rotated 120° from the other [Fig. 1(c)], resulting in a magnetic response which is a superposition of all three. The anisotropy of the Mn^{2+} moments can be strongly modified from in-plane to out-of-plane by less than 1% Li doping in α -MnTe, which also introduces charge carriers into the system [Fig. 1(d)] [30]. This spin reorientation removes the three-fold degeneracy in the magnetic channel, and effectively provides another pathway to achieving a single domain response without modifying the symmetries required for altermagnetism [Fig. 1(e)] [17–19].

Understanding the impact of charge carriers on this prototypical altermagnetic ground state and its excitations is important. The AHE, for example, has been shown to be highly sample-dependent based on the magnitude of the experimental charge gap, revealing a narrow window of in-gap impurity states for which the AHE is observable in α -MnTe [24]. The chiral splitting of the magnons is driven by the difference in the exchange pathways J_{10} and J_{11} which, while equal in distance, are differentiated by the specific pathway through Te orbitals [Fig. 1(a)] [29]. For spin waves in Li-doped α -MnTe, while the spin reorientation is expected to renormalize

the domain contributions and the spin gap induced by SOC [Fig. 1(j-m)], it remains unclear how the addition of charge carriers and the associated structural substitution of Li into the lattice impact the spin dynamics which underlie the functionality of the altermagnetism in this system. To address this, we investigate the effects of 3% Li doping on the spin waves of α -MnTe via single-crystal inelastic neutron scattering (INS) measurements, and present a quantitative comparison of these results with those from undoped α -MnTe.

While spin waves in both undoped and Li-doped α -MnTe can be well-described within a local-moment framework, the addition of charge carriers via Li doping modifies the spin anisotropy gap through SOC [30], induces magnon damping at all energies, and obscures the chiral magnon splitting seen in undoped α -MnTe – all via interactions with itinerant electrons. Therefore, itinerant electron-local moment interactions in α -MnTe are essential not only in determining the AHE [24], but also for understanding spin dynamics in a system dominated by Mn^{2+} local moments.

To determine the position and occupancy of Li atoms, we performed single crystal neutron diffraction measurements and refined several structural models against the

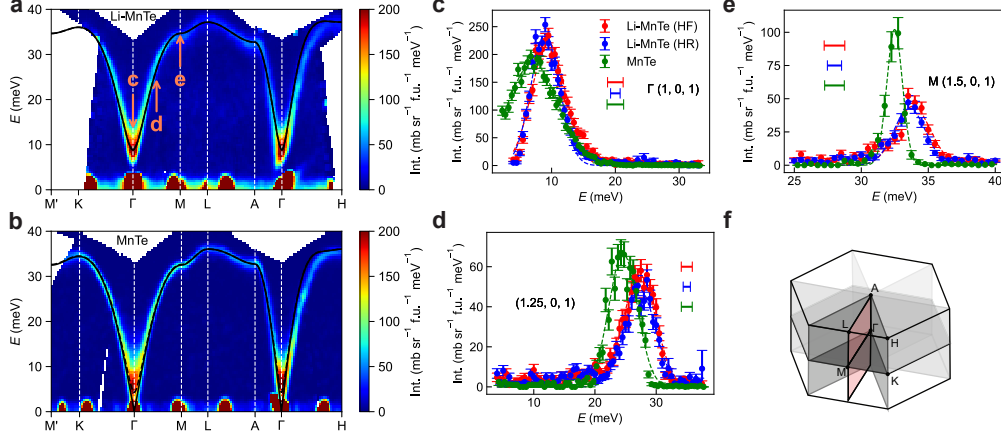


FIG. 2. (a,b) INS spectra acquired at base temperature ($T < 10$ K) with an incident energy of $E_i = 50$ meV for Li-doped [high-flux (HF) mode] and undoped α -MnTe, shown along high-symmetry directions within the nodal plane. The black solid and dashed curves represent calculated spin wave branches, which are degenerate in the Li-doped sample. (c-e) Energy-axis line cuts at selected Q points marked in panel (a), including both HF and high-resolution (HR) modes for Li-doped α -MnTe. Dashed lines indicate Gaussian fits. Horizontal bars mark the instrumental energy resolution at the Gaussian peak position for each configuration. (f) Schematic of the Brillouin zone indicating high-symmetry points. The nodal planes are shown in gray, and the Γ -A-L-M plane is highlighted in red.

experimental data. The results indicate an approximately 4% Te-site deficiency in both samples (Tables S5-S10). In the Li-doped sample, allowing Li to occupy the Te 2c site yields a stable refined Li occupancy of $\sim 3\%$ at both 90 K and 340 K, whereas placing Li on the 2d site or on tested interstitial positions drives the Li occupancy to values that are effectively zero and does not improve the agreement factors (Table S3). While diffraction alone is not sensitive to Li incorporated on uncorrelated interstitial sites, these results suggest that Li is preferentially accommodated on the Te 2c site at a level of $\sim 3\%$. The temperature dependence of the magnetization of the 3% Li-doped sample is consistent with a Néel vector along the c axis [Fig. 1(f)] [30], while the resistivity drops by two orders of magnitude relative to undoped α -MnTe [Fig. 1(g)]. Notably, T_{AM} remains unchanged at this doping level, reminiscent of the robust antiferromagnetic ground state observed in K-doped BaMn_2As_2 [42]. This suggests that the effective exchange energy scale between Mn^{2+} local moments remains similarly unchanged. The extracted carrier density and positive Hall coefficient indicates that holes are the dominant carrier in both systems, and Li doping enhances their contribution to conduction [Fig. 1(h,i)].

To understand the impact of Li-doping on the spin waves of α -MnTe, we conducted INS measurements at the SEQUOIA spectrometer at the Spallation Neutron Source for undoped α -MnTe and at the MAPS Spectrometer at the ISIS Neutron Source for Li-doped α -MnTe. Importantly, both experiments were carried out on a single piece of single crystal with mosaic less than 1 degree using a nearly identical resolution and normalized to absolute units in order to ensure a quantitative compari-

son of the experimental spectra [43]. The chiral magnon splitting for pure α -MnTe is observed in the Γ -A-L-M plane of BZ, highlighted in red in Fig. 2f, while spin waves remain degenerate in the nodal planes shaded in gray [29]. We first examine spin waves along directions in the nodal planes [Fig. 2 (a,b)], which reveal three differences induced by Li doping: (1) the spectra evolve from pseudo-gapless to having a ~ 6 meV spin gap, indicative of the change in single-ion anisotropy, (2) the overall bandwidth of the excitations is reduced from 35 meV to 32 meV, signaling a 9% reduction in the effective exchange energy scale, and (3) whereas spin waves in α -MnTe are resolution-limited in energy, the linewidth in the Li-doped case is substantially broadened [Fig. 2(c-e), S2].

Whereas (2) can be understood as the addition of indirect exchange via Ruderman-Kittel-Kasuya-Yosida (RKKY)-type interactions mediated by itinerant carriers, the Q -independent damping implied by (3) may have several possible physical origins for local moment metals. First, the non-relativistic spin splitting in the electronic bands in altermagnets may allow intra-band spin-flip scattering along certain directions in reciprocal space, giving rise to strongly momentum-dependent magnon broadening. However, spin waves in Li-doped α -MnTe show a relatively Q -independent broadening across the BZ (including nodal planes) and at all energies (Figs. 3(h,i), S2). This stands in sharp contrast to itinerant magnets with comparable metallicity such as MnSi [44–46], FeGe [47], and α -Fe [14–16], where resolution-limited spin waves persist up to the appearance of a Stoner continuum. Second, the quasi-random substitution of Li^+ within the lattice can generate a distribution of local

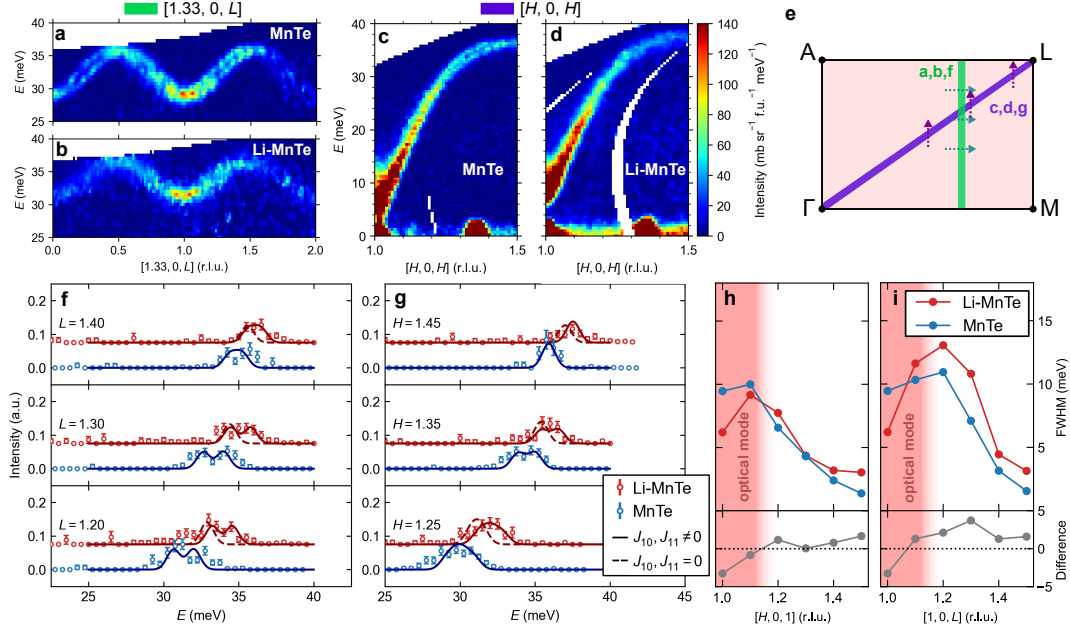


FIG. 3. (a,b) INS spectra along $[1.33, 0, L]$ and (c,d) along the $[H, 0, H]$ direction for undoped and Li-doped α -MnTe. (e) Schematic of the Γ -A-L-M plane of the Brillouin zone, where splitting is expected to occur in undoped α -MnTe. Green and purple lines highlight the $[1.33, 0, L]$ and $[H, 0, H]$ directions, respectively. Arrows indicate the direction of constant- Q line cuts. (f) Comparison of line cuts for the dispersion along the $[1.33, 0, L]$ and (g) $[H, 0, H]$ directions. Points represent the measured data, and error bars represent 1σ uncertainties. Solid and dashed curves represent fits to LSWT models where J_{10} and J_{11} are nonzero and zero, respectively. For Li-doped α -MnTe, the nonzero values of J_{10} and J_{11} were fixed to the refined values from undoped α -MnTe. Data for Li-doped α -MnTe was shifted vertically by 0.075 units for clarity. (h,i) Wavevector dependence of the energy full-width at half-maxima (FWHM) near the zone center $Q_{\Gamma} = (1, 0, 1)$ along Γ -A and Γ -M directions, respectively.

exchange coupling strengths mediated by RKKY interactions, and this exchange disorder can manifest as a smeared energy linewidth reflecting a superposition of the local exchange couplings. We note, however, that the level of disorder between our samples of undoped and Li-doped α -MnTe are nearly comparable. Further, at a doping level of 3% Li per formula unit, there is only a $\sim 15\%$ probability that a given Mn^{2+} would have Li^{+} as a NN [Fig. 1(b)], suggesting that a purely disorder-driven effect is insufficient to describe the strong renormalization of the spin wave lifetime. In electron-doped iron pnictides $\text{BaFe}_{2-x}\text{Ni}_x\text{As}_2$, doping levels up to $x = 0.30$ do not modify the high-energy spin excitations [48], much different from the spin wave broadening seen in the entire BZ of Li-doped α -MnTe [Figs. 3(h,i), S2]. Lastly, magnons may decay into low-energy particle-hole excitations near the Fermi level, as observed in the Mn-based metallic magnets YbMnBi_2 [49] and YbMnSb_2 [50] where a low density of states at the Fermi level results in a Q -independent damping at all energies.

As a measure of the modifications to the spin Hamiltonian within a local moment framework, we fit the spin wave spectra of both compounds using LSWT based on a Heisenberg Hamiltonian with a single-ion anisotropy term D_z (Eqn. S1). A positive (negative) D_z corresponds to the easy-plane (easy-axis) anisotropy in the undoped

(doped) system. Compared to undoped α -MnTe, the NN exchange coupling J_1 in the Li-doped sample is reduced by $\sim 8\%$, consistent with the spin wave bandwidth reduction.

To quantify the effects of an RKKY-mediated exchange-disorder scenario, we assume the spectral weight as a Gaussian distribution with a finite half-width at half-maximum (HWHM) centered around the spin wave dispersion $E(Q)$. While the large linewidths near the Γ point is primarily attributed to overlap between (non-)degenerate optical and acoustic modes, the linewidths at the BZ boundaries more accurately capture the underlying broadening (Fig. S2). Accordingly, we employed three sets of fitted energy values ($E + \text{HWHM}$, E , and $E - \text{HWHM}$) along the M-L and L-A directions, and used E alone along other high-symmetry directions as input for LSWT calculations. These are denoted as “upper”, “center”, and “lower”, respectively, in Table S1. Among the exchange parameters, the further-neighbor interactions and the anisotropy term were found to be relatively insensitive to this spectral weight distribution. In contrast, the J_1 term exhibited a distribution range of ≈ 0.33 meV, corresponding to a HWHM of about 1.5 meV in the spectral weight at the BZ boundary.

We now inspect the spin wave spectra on the Γ -A-L-M plane of the BZ, where splitting is expected for

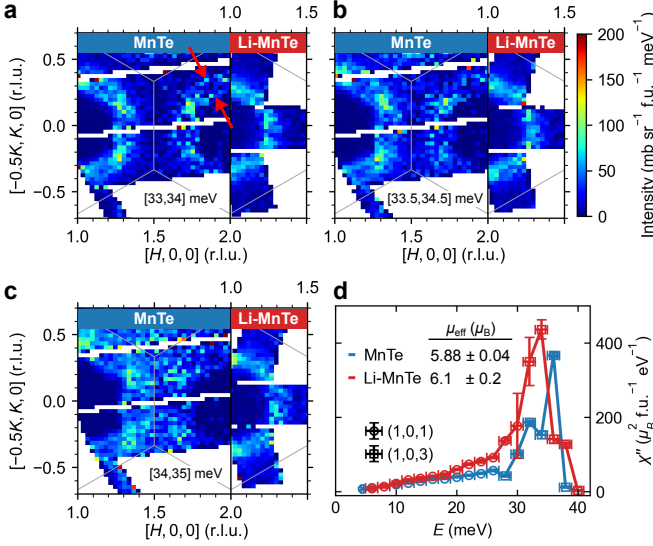


FIG. 4. (a-c) Constant-energy maps of the INS spectra in the HK plane for undoped (left) and Li-doped α -MnTe (right) between 33.5 meV and 34.5 meV. The BZ is outlined by a thin grey line. The observed splitting in undoped α -MnTe is indicated by red arrows. (d) Energy dependence of the local dynamic susceptibility extracted from INS data, with effective moments obtained from the total moment sum rule.

undoped α -MnTe [Fig. 3(e)] [29]. Figure 3(a-d) show a comparison of spin wave spectra along the $[1.33, 0, L]$ and $[H, 0, H]$ directions for both systems. While splitting is clearly observed in undoped α -MnTe [29], the broadened linewidth in Li-doped α -MnTe makes the splitting more challenging to resolve. This is also reflected in constant energy cuts [Fig. 4(a-c)], where inspection of the Q -dependence of the ring-like spectral weight reveals an alternating bright/dim pattern around the ring, which is a direct result of the splitting in undoped α -MnTe. We note that in Li-doped α -MnTe a weak alternation is evident at 34.5 meV, which may signal a weak splitting which survives Li-doping [Fig. 4(c)]. To more closely investigate the presence of splitting in the two systems, we performed constant- Q cuts near the expected splitting position in Q - E space [Fig. 3(e-g)]. While two peaks are resolvable in the line cuts for undoped α -MnTe, the spectra for Li-doped α -MnTe are evidently broader and only a single, broad peak is resolvable for most L values. To understand whether the observed dispersion and lineshape for Li-doped α -MnTe can be explained by a persistent splitting which is simply broadened by the addition of itinerant carriers, we fit the data to two distinct LSWT models with refined J_1, J_2, J_3 : (1) with J_{10} and J_{11} zero, where splitting is necessarily absent; (2) with non-zero difference $J_{10} - J_{11}$ fixed at the value refined for undoped α -MnTe. J_{10} and J_{11} were allowed to refine under this constraint [Fig. 3(f,g)]. In the former scenario, which neglects the splitting allowed by the altermagnetic symmetry, the energy of the spin waves in

Li-doped α -MnTe are underestimated near the expected splitting, and the experimental linewidth is substantially broader than predicted by the model. For the model with $J_{10}, J_{11} \neq 0$, we find improved agreement with experimental energies, further suggesting that the splitting in α -MnTe may survive Li-doping.

While Li-doping strongly modifies the spin anisotropy and tunes the electronic carrier concentration, altermagnetism is, *a priori*, expected to remain robust to a first-order approximation as its framework holds valid for both insulating and metallic systems. The addition of charge carriers to α -MnTe may, however, impact the nature of the magnetic exchange via coupling between itinerant electrons and local moments through RKKY (indirect exchange) interactions and magnon-electron scattering processes. These may shorten the magnon lifetime and therefore explain the broadened linewidth of spin waves throughout the BZ. The absence of a pronounced Q -dependence in the linewidth broadening [Figs. 3(h,i), S2] further supports this interpretation in the low-carrier density limit [49, 50]. The fact that small amounts of Li doping can dramatically affect the spin gap and the spin waves bandwidth is also supportive of the important role of itinerant electrons in this system. The sensitive dependence of the AHE on the charge gap in undoped α -MnTe [24] further underscores the notion that the physics of this system is best described as a network of local moments that interact with itinerant charge carriers.

We further test this notion by calculating the local dynamic susceptibility from the total spectral weight of our INS measurements [Fig. 4(d)], which, when integrated across all energy transfers, yields a quantitative measure of the local dynamic moment [43, 48]. This yields a dynamic moment of $1.53(1) \mu_B$ [$1.84(6) \mu_B$] for undoped α -MnTe [Li-doped α -MnTe] which, when combined with the corresponding static ordered moment following the total moment sum rule (Eqn. S2), indicates a total effective moment of $5.88(4) \mu_B$ [$6.1(2) \mu_B$]. These values are close to the expected $\mu_{\text{eff}} = 5.9 \mu_B$ for $S = 5/2$ ($\gg S = 1/2$) Mn^{2+} ions, therefore strongly suggesting a local moment picture for altermagnetism in both compounds, while the addition of itinerant electrons serves to modify interactions between the Mn^{2+} spins.

In comparing Li-doped and undoped α -MnTe, we find well-defined spin waves throughout the BZ with broadened energy width induced by Li doping. This is reminiscent of the broadened spin waves in ferromagnetic CrGeTe_3 due to dynamical spin-lattice coupling arising from the zero-temperature lattice vibration [51]. Since spin-lattice coupling should be similar for undoped and Li-doped α -MnTe, the observed spin wave broadening and damping in Li-doped α -MnTe must arise from Li-doping-induced itinerant electron-local moment interactions which must be considered to understand the physics of altermagnetic candidate materials.

ACKNOWLEDGMENTS

We thank Kirill Belashchenko for helpful discussions. The single-crystal synthesis and neutron scattering work at Rice were supported by the U.S. DOE, BES under Grant Nos. DE-SC0012311 (P.D.) and DE-SC0026179 (P.D., E.M.). Part of the materials characterization efforts at Rice is supported by the Robert A. Welch Foundation Grant No. C-1839 (P.D.). X.W. acknowledges research sponsored by the Laboratory Directed Research and Development Program of ORNL, managed by UT-Battelle, LLC, for the U.S. DOE. Part of the materials characterization efforts at University of Houston is supported by the T. L. L. Temple Foundation; the John J and Rebecca Moores Endowment; the State of Texas through the Texas Center for Superconductivity at the University of Houston; and the Robert A. Welch Foundation (00730-5021-H0452-B0001-G0512489). A portion of this research used resources at the Spallation Neutron Source, a DOE Office of Science User Facility operated by ORNL. The beam times were allocated to TOPAZ and SEQUOIA on Proposals No. IPTS-35052, IPTS-33830 and IPTS-34120. The experiment at the ISIS Neutron and Muon Source was supported by beam time allocations RB2510033 and RB2510079 from the Science and Technology Facilities Council. The data supporting this manuscript are available from the authors upon reasonable request.

[†] These authors contributed equally to this work.

* pdai@rice.edu

- [1] W. Heisenberg, *Zeitschrift Fur Physik* **49**, 619 (1928).
- [2] T. Holstein and H. Primakoff, *Phys. Rev.* **58**, 1098 (1940).
- [3] T. Oguchi, *Phys. Rev.* **117**, 117 (1960).
- [4] A. T. Boothroyd, *Principles of Neutron Scattering from Condensed Matter* (Oxford University Press, 2020).
- [5] M. E. Zhitomirsky and A. L. Chernyshev, *Rev. Mod. Phys.* **85**, 219 (2013).
- [6] O. W. Dietrich, J. Als-Nielsen, and L. Passell, *Phys. Rev. B* **14**, 4923 (1976).
- [7] S. P. Bayrakci, D. A. Tennant, P. Leininger, T. Keller, M. C. R. Gibson, S. D. Wilson, R. J. Birgeneau, and B. Keimer, *Phys. Rev. Lett.* **111**, 017204 (2013).
- [8] E. C. Stoner, *Proc. R. Soc. A* **154**, 656 (1936).
- [9] E. C. Stoner, *Proc. R. Soc. A* **165**, 372 (1938).
- [10] J. C. Slater, *Phys. Rev.* **52**, 198 (1937).
- [11] E. P. Wohlfarth, *Rev. Mod. Phys.* **25**, 211 (1953).
- [12] L. Landau and E. Lifshitz, *Phys. Z. Sowjetunion* **8**, 153 (1935).
- [13] T. L. Gilbert, *Bull. Am. Phys. Soc. II*, **30**, 19 (1955).
- [14] J. W. Lynn, *Phys. Rev. B* **11**, 2624 (1975).
- [15] T. G. Perring, A. T. Boothroyd, D. M. Paul, A. D. Taylor, R. Osborn, R. J. Newport, J. A. Blackman, and H. A. Mook, *Journal of Applied Physics* **69**, 6219 (1991).
- [16] N. B. Brookes, D. Betto, K. Cao, Y. Lu, K. Kummer, and F. Giustino, *Phys. Rev. B* **102**, 064412 (2020).
- [17] L. Šmejkal, R. González-Hernández, T. Jungwirth, and J. Sinova, *Sci. Adv.* **6**, eaaz8809 (2020).
- [18] L. Šmejkal, *Phys. Rev. X* **12**, 10.1103/PhysRevX.12.031042 (2022).
- [19] L. Šmejkal, *Phys. Rev. X* **12**, 040501 (2022).
- [20] A. D. Din, D. Usanov, L. Šmejkal, S. D'Souza, F. Guo, O. Amin, E. Dawa, R. Campion, K. Edmonds, B. Kiraly, *et al.*, arXiv:2511.01690 (2025).
- [21] R. Gonzalez Betancourt, J. Zubáč, R. Gonzalez-Hernandez, K. Geishendorf, Z. Šobáň, G. Springholz, K. Olejník, L. Šmejkal, J. Sinova, T. Jungwirth, S. Goennenwein, A. Thomas, H. Reichlová, J. Železný, and D. Kriegner, *Phys. Rev. Lett.* **130**, 036702 (2023).
- [22] K. P. Kluczyk, K. Gas, M. J. Grzybowski, P. Skupieński, M. A. Borysiewicz, T. Faş, J. Suffczyński, J. Z. Domagala, K. Graszka, A. Mycielski, M. Baj, K. H. Ahn, K. Výborný, M. Sawicki, and M. Gryglas-Borysiewicz, *Phys. Rev. B* **110**, 155201 (2024).
- [23] K. D. Belashchenko, *Phys. Rev. Lett.* **134**, 086701 (2025).
- [24] Z. Liu, S. Xu, J. M. DeStefano, E. Rosenberg, T. Zhang, J. Li, M. B. Stone, F. Ye, R. Cong, S. Pan, C.-W. Chu, L. Deng, E. Morosan, R. M. Fernandes, J.-H. Chu, and P. Dai, arXiv:2509.19582 (2025).
- [25] S. Smolenski, N. Mao, D. Zhang, Y. Guo, A. K. M. A. Shawon, M. Xu, E. Downey, T. Musall, M. Yi, W. Xie, C. Jozwiak, A. Bostwick, N. Tamura, E. Rotenberg, L. Li, K. Sun, Y. Zhang, and N. H. Jo, arXiv:2509.21481 (2025).
- [26] A. Hariki, A. Dal Din, O. Amin, T. Yamaguchi, A. Badura, D. Kriegner, K. Edmonds, R. Campion, P. Wadley, D. Backes, L. Veiga, S. Dhesi, G. Springholz, L. Šmejkal, K. Výborný, T. Jungwirth, and J. Kuneš, *Phys. Rev. Lett.* **132**, 176701 (2024).
- [27] A. Barman, G. Gubbiotti, S. Ladak, A. O. Adeyeye, M. Krawczyk, J. Gräfe, C. Adelman, S. Coto-fana, A. Naeemi, V. I. Vasyuchka, B. Hillebrands, S. A. Nikitov, H. Yu, D. Grundler, A. V. Sadovnikov, A. A. Grachev, S. E. Sheshukova, J.-Y. Duquesne, M. Marangolo, G. Csaba, W. Porod, V. E. Demidov, S. Urazhdin, S. O. Demokritov, E. Albisetti, D. Petti, R. Bertacco, H. Schultheiss, V. V. Kruglyak, V. D. Poimanov, S. Sahoo, J. Sinha, H. Yang, M. Münzenberg, T. Moriyama, S. Mizukami, P. Landeros, R. A. Gallardo, G. Carlotti, J.-V. Kim, R. L. Stamps, R. E. Camley, B. Rana, Y. Otani, W. Yu, T. Yu, G. E. W. Bauer, C. Back, G. S. Uhrig, O. V. Dobrovolskiy, B. Budinska, H. Qin, S. van Dijken, A. V. Chumak, A. Khitun, D. E. Nikonov, I. A. Young, B. W. Zingsem, and M. Winklhofer, *J. Phys.: Condens. Matter* **33**, 413001 (2021).
- [28] B. Flebus, D. Grundler, B. Rana, Y. Otani, I. Barsukov, A. Barman, G. Gubbiotti, P. Landeros, J. Akerman, U. Ebels, P. Pirro, V. E. Demidov, K. Schultheiss, G. Csaba, Q. Wang, F. Ciubotaru, D. E. Nikonov, P. Che, R. Hertel, T. Ono, D. Afanasiev, J. Mentink, T. Rasing, B. Hillebrands, S. V. Kusminskiy, W. Zhang, C. R. Du, A. Finco, T. van der Sar, Y. K. Luo, Y. Shiota, J. Sklenar, T. Yu, and J. Rao, *J. Phys.: Condens. Matter* **36**, 363501 (2024).
- [29] Z. Liu, M. Ozeki, S. Asai, S. Itoh, and T. Masuda, *Phys. Rev. Lett.* **133**, 156702 (2024).
- [30] G. Yumnam, D. H. Moseley, J. A. M. Paddison, C. Z. Suggs, E. Zappala, D. S. Parker, G. E. Granroth, G. D.

- Morris, M. M. H. Polash, D. Vashae, M. A. McGuire, H. Zhao, M. E. Manley, B. A. Frandsen, and R. P. Hermann, *Phys. Rev. B* **109**, 214434 (2024).
- [31] D. H. Moseley, K. M. Taddei, J. Yan, M. A. McGuire, S. Calder, M. M. H. Polash, D. Vashae, X. Zhang, H. Zhao, D. S. Parker, R. S. Fishman, and R. P. Hermann, *Phys. Rev. Mater.* **6**, 014404 (2022).
- [32] D. Kriegner, K. Výborný, K. Olejník, H. Reichlová, V. Novák, X. Marti, J. Gazquez, V. Saidl, P. Němec, V. V. Volobuev, G. Springholz, V. Holý, and T. Jungwirth, *Nat. Commun.* **7**, 11623 (2016).
- [33] D. Kriegner, H. Reichlova, J. Grenzer, W. Schmidt, E. Ressouche, J. Godinho, T. Wagner, S. Y. Martin, A. B. Shick, V. V. Volobuev, G. Springholz, V. Holý, J. Wunderlich, T. Jungwirth, and K. Výborný, *Phys. Rev. B* **96**, 214418 (2017).
- [34] O. J. Amin, A. Dal Din, E. Golias, Y. Niu, A. Zakharov, S. C. Fromage, C. J. B. Fields, S. L. Heywood, R. B. Cousins, F. Maccherozzi, J. Krempaský, J. H. Dil, D. Kriegner, B. Kiraly, R. P. Campion, A. W. Rushforth, K. W. Edmonds, S. S. Dhesi, L. Šmejkal, T. Jungwirth, and P. Wadley, *Nature* **636**, 348 (2024).
- [35] R. D. Gonzalez Betancourt, J. Zubáč, K. Geishendorf, P. Ritzinger, B. Růžicková, T. Kotte, J. Železný, K. Olejník, G. Springholz, B. Büchner, A. Thomas, K. Výborný, T. Jungwirth, H. Reichlová, and D. Kriegner, *npj Spintronics* **2**, 45 (2024).
- [36] J. Dzian, P. Kubaščík, S. Tázlarů, M. Białek, M. Šindler, F. Le Mardele, C. Kadlec, F. Kadlec, M. Gryglas-Borysiewicz, K. P. Kluczyk, A. Mycielski, P. Skupiński, J. Hejtmánek, R. Tesař, J. Železný, A.-L. Barra, C. Faugeras, J. Volný, K. Uhlířová, L. Nádvorník, M. Veis, K. Výborný, and M. Orlita, *Phys. Rev. B* **112**, 024433 (2025).
- [37] N. Kunitomi, Y. Hamaguchi, and S. Anzai, *J. Phys. France* **25**, 568 (1964).
- [38] J. B. C. Efreem D'Sa, P. A. Bhobe, K. R. Priolkar, A. Das, S. K. Paranjpe, R. B. Prabhu, and P. R. Sarode, *J. Magn. Magn. Mater.* **285**, 267 (2005).
- [39] W. Szuszkiewicz, B. Hennion, B. Witkowska, E. Łusakowska, and A. Mycielski, *physica status solidi (c)* **2**, 1141 (2005).
- [40] D. Kriegner, H. Reichlova, J. Grenzer, W. Schmidt, E. Ressouche, J. Godinho, T. Wagner, S. Y. Martin, A. B. Shick, V. V. Volobuev, G. Springholz, V. Holý, J. Wunderlich, T. Jungwirth, and K. Výborný, *Phys. Rev. B* **96**, 214418 (2017).
- [41] W. Szuszkiewicz, E. Dynowska, B. Witkowska, and B. Hennion, *Phys. Rev. B* **73**, 104403 (2006).
- [42] J. Lamsal, G. S. Tucker, T. W. Heitmann, A. Kreyssig, A. Jesche, A. Pandey, W. Tian, R. J. McQueeney, D. C. Johnston, and A. I. Goldman, *Phys. Rev. B* **87**, 144418 (2013).
- [43] G. Xu, Z. Xu, and J. M. Tranquada, *Review of Scientific Instruments* **84**, 083906 (2013).
- [44] A. E. Petrova, E. D. Bauer, V. Krasnorussky, and S. M. Stishov, *Phys. Rev. B* **74**, 092401 (2006).
- [45] Y. Ishikawa, G. Shirane, J. A. Tarvin, and M. Kohgi, *Phys. Rev. B* **16**, 4956 (1977).
- [46] X. Chen, I. Krivenko, M. B. Stone, A. I. Kolesnikov, T. Wolf, D. Reznik, K. S. Bedell, F. Lechermann, and S. D. Wilson, *Nat. Commun.* **11**, 3076 (2020).
- [47] X. Teng, D. W. Tam, L. Chen, H. Tan, Y. Xie, B. Gao, G. E. Granroth, A. Ivanov, P. Bourges, B. Yan, M. Yi, and P. Dai, *Phys. Rev. Lett.* **133**, 046502 (2024).
- [48] P. Dai, *Rev. Mod. Phys.* **87**, 855 (2015).
- [49] A. Sapkota, L. Classen, M. B. Stone, A. T. Savici, V. O. Garlea, A. Wang, J. M. Tranquada, C. Petrovic, and I. A. Zaliznyak, *Phys. Rev. B* **101**, 041111 (2020).
- [50] X. Hu, A. Sapkota, Z. Hu, A. T. Savici, A. I. Kolesnikov, J. M. Tranquada, C. Petrovic, and I. A. Zaliznyak, *Phys. Rev. B* **107**, L201117 (2023).
- [51] L. Chen, C. Mao, J.-H. Chung, M. B. Stone, A. I. Kolesnikov, X. Wang, N. Murai, B. Gao, O. Delaire, and P. Dai, *Nat. Commun.* **13**, 4037 (2022).
- [52] L. Coates, H. Cao, B. C. Chakoumakos, M. D. Frontzek, C. Hoffmann, A. Y. Kovalevsky, Y. Liu, F. Meilleur, A. M. dos Santos, D. A. Myles, *et al.*, *Rev. Sci. Instrum.* **89** (2018).
- [53] Oak Ridge National Laboratory, Neuxtalviz, <https://single-crystal.ornl.gov/software/neuxtalviz/index.html>, accessed: 2025-11-25.
- [54] V. Reshniak, X. Wang, G. Zhang, S. Liu, and J. Yin, *arXiv preprint arXiv:2406.05133* (2024).
- [55] A. J. Schultz, M. R. V. Jørgensen, X. Wang, R. L. Mikkelsen, D. J. Mikkelsen, V. E. Lynch, P. F. Peterson, M. L. Green, and C. M. Hoffmann, *J. Appl. Crystallogr.* **47**, 915 (2014).
- [56] G. M. Sheldrick, *Acta Crystallogr. C* **71**, 3 (2015).
- [57] V. Petříček, L. Palatinus, J. Plášil, and M. Dušek, *Zeitschrift für Kristallographie-Crystalline Materials* **238**, 271 (2023).
- [58] G. E. Granroth, D. H. Vandergriff, and S. E. Nagler, *Physica B* **385**, 1104 (2006).
- [59] G. Granroth, A. Kolesnikov, T. Sherline, J. Clancy, K. Ross, J. Ruff, B. Gaulin, and S. Nagler, in *J. Phys.: Conf. Ser.*, Vol. 251 (2010) p. 012058.
- [60] R. Ewings, J. Stewart, T. Perring, R. Bewley, M. Le, D. Raspino, D. Pooley, G. Škoro, S. Waller, D. Zacek, *et al.*, *Rev. Sci. Instrum.* **90** (2019).
- [61] O. Arnold, J.-C. Bilheux, J. Borreguero, A. Buts, S. I. Campbell, L. Chapon, M. Doucet, N. Draper, R. F. Leal, M. Gigg, *et al.*, *Nuclear instruments and methods in physics research section a: accelerators, spectrometers, detectors and associated equipment* **764**, 156 (2014).
- [62] R. Ewings, A. Buts, M. Le, J. van Duijn, I. Bustinduy, and T. Perring, *Nuclear Instruments and Methods in Physics Research Section A: Accelerators, Spectrometers, Detectors and Associated Equipment* **834**, 132 (2016).
- [63] A. S. (ORNL) and I. Z. (BNL), *Shiver software* (2019).
- [64] S. Toth and B. Lake, *J. Phys.: Condens. Matter* **27**, 166002 (2015).

Supplemental Information

EXPERIMENTAL DETAILS

Sample synthesis and characterization

Single crystals of α -MnTe and Li-doped α -MnTe were synthesized using Te self-flux method following the procedures as described in our previous work [24]. Magnetic susceptibility measurements were performed on a single-crystal Li-doped α -MnTe sample with a mass of 90.4 mg, using a Quantum Design Magnetic Property Measurement System (MPMS) equipped with a superconducting quantum interference device (SQUID) magnetometer. The sample was mounted on the sample holder using GE varnish. Both field-cooled (FC) and zero-field-cooled (ZFC) measurements were conducted with the magnetic field applied along the c -axis and within the ab -plane.

Neutron diffraction

Neutron diffraction measurements were carried out using the single crystal diffractometer TOPAZ at the Spallation Neutron Source (SNS), Oak Ridge National Laboratory (ORNL) [52]. The experiments employed a broad neutron wavelength range of 0.4–3.5 Å. Single crystals of Li-doped α -MnTe (~ 100 mg) and pure α -MnTe (~ 50 mg) were used. The samples were mounted on the ambient goniometer, and data were collected using time-of-flight (TOF) techniques, which provided wavelength-resolved Laue diffraction patterns. Diffraction datasets for both samples were obtained at 90 K and 340 K. A nitrogen cryostream was utilized for temperature control.

The data collection strategy was determined using the planning tool in NeuXtalViz [53]. A multiresolution machine learning method was employed for peak integration to obtain peak intensities in three-dimensional (H, K, L) space [54]. Data reduction and normalization, including the Lorentz factor, neutron TOF spectrum, and detector efficiency corrections, were carried out following the procedure reported previously [55]. The reduced data were saved in SHELX HKLF2 format [56] with the neutron wavelength recorded separately for each reflection. The neutron crystal structures were solved in JANA2020 [57] and refined successfully to convergence.

The momentum transfer \mathbf{Q} in 3D reciprocal space is defined as $\mathbf{Q} = H\mathbf{a}^* + K\mathbf{b}^* + L\mathbf{c}^*$ where H , K and L are Miller indices and $\mathbf{a}^* = 2\pi(\mathbf{b} \times \mathbf{c})/[\mathbf{a} \cdot (\mathbf{b} \times \mathbf{c})]$, $\mathbf{b}^* = 2\pi(\mathbf{c} \times \mathbf{a})/[\mathbf{a} \cdot (\mathbf{b} \times \mathbf{c})]$, $\mathbf{c}^* = 2\pi(\mathbf{a} \times \mathbf{b})/[\mathbf{a} \cdot (\mathbf{b} \times \mathbf{c})]$ with $\mathbf{a} = a\hat{x}$, $\mathbf{b} = a(-1/2 \hat{x} + \sqrt{3}/2 \hat{y})$ and $\mathbf{c} = c\hat{z}$.

Inelastic neutron scattering

Inelastic neutron scattering (INS) measurements on undoped α -MnTe and preliminary measurements on Li-doped α -MnTe were performed using the fine-resolution Fermi chopper spectrometer SEQUOIA at the Spallation Neutron Source (SNS), Oak Ridge National Laboratory (ORNL) [58, 59]. For the pure α -MnTe sample, a single crystal with a mass of approximately 0.46 g was mounted in the $[H, 0, L]$ scattering plane. Data were collected at $T = 8$ K using an incident energy of $E_i = 50$ meV with the high-flux chopper operating at a frequency of $f = 180$ Hz. Measurements were performed over a total rotation range of 120 degrees about the vertical axis of the sample, with a step size of 0.5 degrees. During the experiment, the SNS accelerator operated at a beam power of 1.8 MW, and data were collected for an accumulated proton charge of approximately 0.4 Coulombs per angle step, corresponding to a counting time of roughly 5 minutes. The data obtained from SEQUOIA are presented in Figs. 2(b)–(e), 3(a)(c)(f)–(i), 4, and S2.

For the Li-doped α -MnTe sample, an early-stage experiment was conducted at $T = 6$ K using an array of co-aligned crystals with a total mass of approximately 0.4 g, also mounted in the $[H, 0, L]$ scattering plane. Several experimental configurations were employed: high-flux mode with incident energy $E_i = 50$ meV at Fermi frequency $f = 300$ Hz and $E_i = 25$ meV at $f = 240$ Hz, as well as high-resolution mode with $E_i = 60$ meV at $f = 420$ Hz.

INS measurements on Li-doped α -MnTe were carried out using the TOF spectrometer MAPS at the ISIS Neutron and Muon Source, Rutherford Appleton Laboratory [60]. The sample, with a mass of approximately 2.2 g, was obtained from the same large single crystal used for the TOPAZ experiment and was mounted in the $[H, 0, L]$ scattering plane. Data were collected at $T = 5$ K with an incident energy of $E_i = 50$ meV under continuous rotation about the vertical axis of the sample. During the measurements, the accelerator operated with a synchrotron current of 152 μ A on target station 1. Measurements were carried out in two modes: high-resolution (HR) mode with a Fermi chopper frequency of $f = 300$ Hz and a sample rotation range of 60 degrees, and high-flux (HF) mode with

$f = 150$ Hz and a rotation range of 120 degrees. Each mode was allocated approximately 60 hours of beamtime, evenly distributed over the full angle range. The data were reduced into .nxspe files using a step of 0.5 degrees. Data from the HF mode are presented in Figs. 2(a)(c)–(e), 3(b)(d)(f)–(i), 4, and S2, while data from the HR mode are shown in Figs. 2(c)–(e), S3, and S4.

Data reduction was performed using MANTID [61], Horace [62], and SHIVER [63].

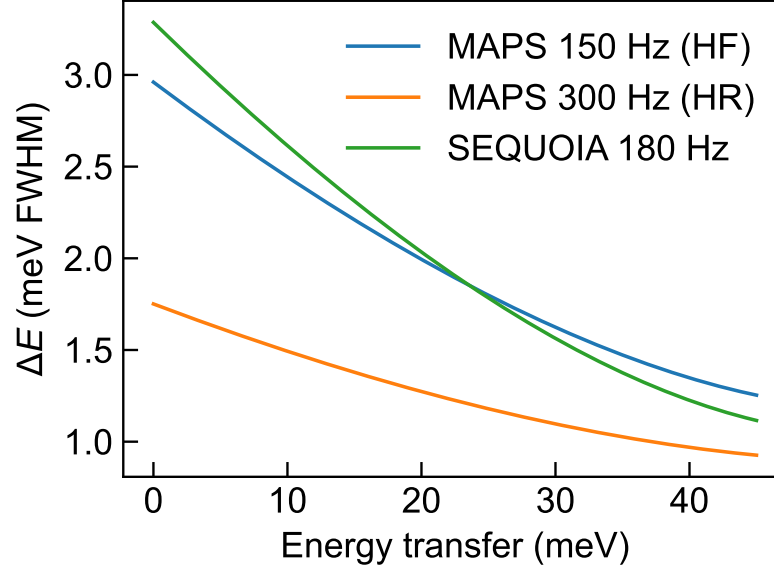


FIG. S1. Energy resolutions calculated using PyChop for the three experimental configurations used to measure the spin excitation data presented in this Letter. HF: high-flux mode; HR: high-resolution mode.

Absolute unit normalization

INS data were normalized to absolute units during the data reduction process by measuring a standard vanadium sample of known mass [43]. The vanadium measurements were performed in the same sample environment and with the same chopper and instrument settings as the sample measurements.

Linear spin wave theory (LSWT) Calculations

The spin Hamiltonian was determined from the INS spectra using linear spin wave theory (LSWT) implemented in the SpinW package [64]. For both compounds, a Heisenberg spin Hamiltonian with a single-ion anisotropy term was employed, expressed as

$$H = \sum_{\langle i,j \rangle} J_{ij} \mathbf{S}_i \cdot \mathbf{S}_j + \sum_i D_z (S_i^z)^2, \quad (1)$$

where i indexes the Mn^{2+} ions, \mathbf{S}_i is the spin operator at site i , and S_i^z denotes its z component. J_{ij} represents the exchange interaction between spins at sites i and j , with the summation taken over spin pairs. In this coordinate system, the z -axis corresponds to the crystallographic c -axis. The anisotropy term D_z is positive for easy-plane anisotropy, as in the case of pure α -MnTe, and negative for Ising-type anisotropy, as observed in Li-doped α -MnTe. To obtain the spin wave dispersion relation $E(\mathbf{Q})$, we performed Gaussian fitting to extract the energy center E and its half-width at half-maximum (HWHM) at each wave vector \mathbf{Q} along high-symmetry directions.

TABLE S1. Exchange coupling constants calculated using SpinW.

Sample and data	J_1	J_2	J_3	D_z	J_{10}	J_{11} (meV)
Pure α -MnTe	3.8951	-0.139	0.46383	0.05519	-0.01378	0.03986
Li-doped α -MnTe upper	3.6575	-0.18698	0.47811	-0.2411		
Li-doped α -MnTe center	3.5909	-0.22146	0.45177	-0.24515		N/A
Li-doped α -MnTe lower	3.3283	-0.21053	0.47816	-0.24695		

Electrical transport measurements

The longitudinal and Hall resistivities were measured using a standard five-probe configuration. Measurements were performed in a 9 T Quantum Design PPMS DynaCool system. The voltage signals were first amplified by appropriate preamplifiers (SR554) and subsequently read out using SR830 lock-in amplifiers. The sample was polished into a bar with dimensions of about $2.0 \times 1.0 \times 0.1$ mm³. During the measurements, the magnetic field was applied along the crystallographic axis $[0, 0, 1]$, while the electrical current flowed along the $[1, 1, 0]$ direction. All field-dependent data were symmetrized and antisymmetrized to correct for contact misalignment.

SINGLE CRYSTAL NEUTRON DIFFRACTION

Experiment and refinement details

TABLE S2. α -MnTe at both temperatures. At 90 K, two magnetic structures were tested.

T	90 K		340 K
Space group	$P6_3/mmc$ (No. 194)		
Magnetic space group	$Cm'c'm$	$Cmcm$	N/A
a (Å)	4.1300(5)		4.1522(5)
c (Å)	6.6530(11)		6.7162(11)
V (Å ³)	98.28(2)		100.28(2)
Index range	$-8 < H < 9$ $-8 < K < 9$ $-14 < L < 14$		$-9 < H < 8$ $-8 < K < 9$ $-14 < L < 14$
Reflections collected ($N(\text{obs})/N(\text{all})$)	2137/2154		1460/1468
R indices ($I > 3\sigma(I)$)	$R=3.57$ $wR2=10.89$	$R=3.47$ $wR2=9.97$	$R=3.13$ $wR2=7.69$
R indices (all data)	$R=3.63$ $R=10.92$	$R=3.52$ $wR2=10.01$	$R=3.16$ $wR2=7.70$
Goodness-of-fit	2.84		1.85
Moment size (μ_B)	4.35(3)		N/A

For α -MnTe, we also evaluated the possibility of intersite mixing, specifically the occupation of Te sites by Mn atoms, using the neutron diffraction dataset collected at 340 K. However, this model did not yield an improved refinement compared to the current model, which assumes that defects are restricted to Te sites and that Mn atoms exclusively occupy their designated lattice positions.

To determine the magnetic structure, two models were tested using the dataset obtained at 90 K. The first model adopts the magnetic space group $Cmcm$, where the magnetic moments align along the crystallographic a axis. The second model corresponds to the magnetic space group $Cm'c'm$, in which the moments are oriented along the reciprocal a^* axis. Although the $Cmcm$ model yielded a slightly better refinement result, the $Cm'c'm$ model is more consistent with our previous neutron diffraction results under strain-induced detwinning of magnetic domains [24].

TABLE S3. Li-doped α -MnTe at 340 K. Models placing Li at Wyckoff site $2c$, site $2d$, or uncorrelated interstitial sites were tested.

Li site	$2c$	$2d$	Uncorrelated
Space group	$P6_3/mmc$ (No. 194)		
a	4.1532(3)		
c	6.7190(8)		
V	100.369(16)		
Index range	$-9 < H < 9$ $-7 < K < 8$ $-13 < L < 14$		
Reflections collected ($N(\text{obs})/N(\text{all})$)	1980/2002		
R indices ($I > 3\sigma(I)$)	$R=3.52$ $wR2=11.76$	$R=3.51$ $wR2=11.76$	$R=3.52$ $wR2=11.76$
R indices (all data)	$R=3.60$ $wR2=11.78$	$R=3.59$ $wR2=11.78$	$R=3.60$ $wR2=11.78$
Goodness-of-fit	2.99	2.99	3.00

We used the 340 K diffraction dataset to investigate the possible crystallographic location of Li atoms. As a first scenario, we considered the possibility that Li atoms occupy uncorrelated interstitial sites. In this case, the Li atoms would not contribute coherent scattering, and therefore the Bragg peak intensities would remain unaffected. Accordingly, Li atoms were not included in the refinement model for this scenario.

We then tested alternative models incorporating Li atoms at crystallographic sites. Both the $2d$ and $2c$ positions (the latter coinciding with Te sites) yielded stable refinements. However, when Li atoms were placed at the $2d$ site, the refined concentration was significantly lower than the nominal doping level of 5%, as shown in Table S9. A similar analysis using the 90 K dataset produced negative Li occupancies at the $2d$ site when the atomic displacement parameters (ADPs) were not constrained, which is physically implausible.

In contrast, assigning Li atoms to the $2c$ site resulted in stable refinements at both temperatures, with a consistent refined concentration of approximately 3%, suggesting that the $2c$ site is a more plausible position for Li incorporation.

Nevertheless, we note that the inclusion of Li atoms at either site did not significantly improve the overall refinement quality (Table S3). Therefore, the possibility that Li atoms reside at random interstitial positions cannot be ruled out.

TABLE S4. Li-doped α -MnTe at 90 K.

Magnetic space group	$P6_3/m'm'c$	$Cm'cm'$
Space group	$P6_3/mmc$ (No. 194)	
a	4.130(2)	
c	6.666(2)	
V	98.48(7)	
Index range	$-9 < H < 9$ $-7 < K < 8$ $-13 < L < 14$	
Reflections collected ($N(\text{obs})/N(\text{all})$)	3215/3261	
R indices ($I > 3\sigma(I)$)	$R=4.65$ $wR2=16.04$	$R=4.71$ $wR2 = 16.14$
R indices (all data)	$R=4.71$ $wR2=16.06$	$R = 4.76$ $wR2=16.16$
Goodness-of-fit	4.27	4.30
Moment size (μ_B)	4.29(3)	4.30(10)

In accordance with previous powder neutron diffraction studies [31], we applied the orthorhombic magnetic space group $Cm'cm'$ to refine the magnetic structure of Li-doped α -MnTe. This model also yielded a vanishingly small in-plane magnetic moment at the given doping level. In addition, we tested a hexagonal magnetic space group with higher symmetry, in which the magnetic structure is strictly antiferromagnetic and the magnetic moments are constrained to lie along the crystallographic c axis. The refinement results for both models are summarized in Table S4.

Fractional atomic coordinates and displacement parameter (\AA^2) determined from neutron diffraction

TABLE S5. MnTe, 340 K

Atom	Label	x	y	z	Occ.	$U_{\text{iso}}/U_{\text{eq}}$	Site	Sym.
Mn	Mn1	0	0	0	1.000	0.017	2a	$3m$
Te	Te1	1/3	2/3	1/4	0.967(2)	0.010	2c	$\bar{6}m2$

TABLE S6. MnTe, 90 K

Atom	Label	x	y	z	Occ.	$U_{\text{iso}}/U_{\text{eq}}$	Site	Sym.
Mn	Mn1	0	0	0	1.000	0.004	2a	$3m$
Te	Te1	1/3	2/3	1/4	0.957(2)	0.002	2c	$\bar{6}m2$

TABLE S7. Li-doped α -MnTe, without Li atoms

Atom	Label	x	y	z	Occ.	$U_{\text{iso}}/U_{\text{eq}}$	Site	Sym.
Mn	Mn1	0	0	0	1.000	0.017	2a	$3m$
Te	Te1	1/3	2/3	1/4	0.961(3)	0.010	2c	$\bar{6}m2$

TABLE S8. Li-doped α -MnTe, 340 K with the assumption at Li atoms sit at the Te site

Atom	Label	x	y	z	Occ.	$U_{\text{iso}}/U_{\text{eq}}$	Site	Sym.
Mn	Mn1	0	0	0	1.000	0.017	2a	$3m$
Te	Te1	1/3	2/3	1/4	0.970(1)	0.010	2c	$\bar{6}m2$
Li	Li1	1/3	2/3	1/4	0.030(1)	0.010	2c	$\bar{6}m2$

TABLE S9. Li-doped α -MnTe, 340 K with the assumption at Li atoms sit at the 2d site

Atom	Label	x	y	z	Occ.	$U_{\text{iso}}/U_{\text{eq}}$	Site	Sym.
Mn	Mn1	0	0	0	1.000	0.018	2a	$3m$
Te	Te1	1/3	2/3	1/4	0.962(4)	0.010	2c	$\bar{6}m2$
Li	Li1	1/3	2/3	3/4	0.007(16)	0.041	2d	$\bar{6}m2$

TABLE S10. Li-doped α -MnTe, 90 K with the assumption at Li atoms sit at the Te site

Atom	Label	x	y	z	Occ.	$U_{\text{iso}}/U_{\text{eq}}$	Site	Sym.
Mn	Mn1	0	0	0	1.000	0.004	2a	$3m'$
Te	Te1	1/3	2/3	1/4	0.969(2)	0.002	2c	$\bar{6}'m'2$
Li	Li1	1/3	2/3	1/4	0.031(2)	0.002	2c	$\bar{6}'m'2$

SURVEY OF MAGNON LINEWIDTH ACROSS THE BRILLOUIN ZONE

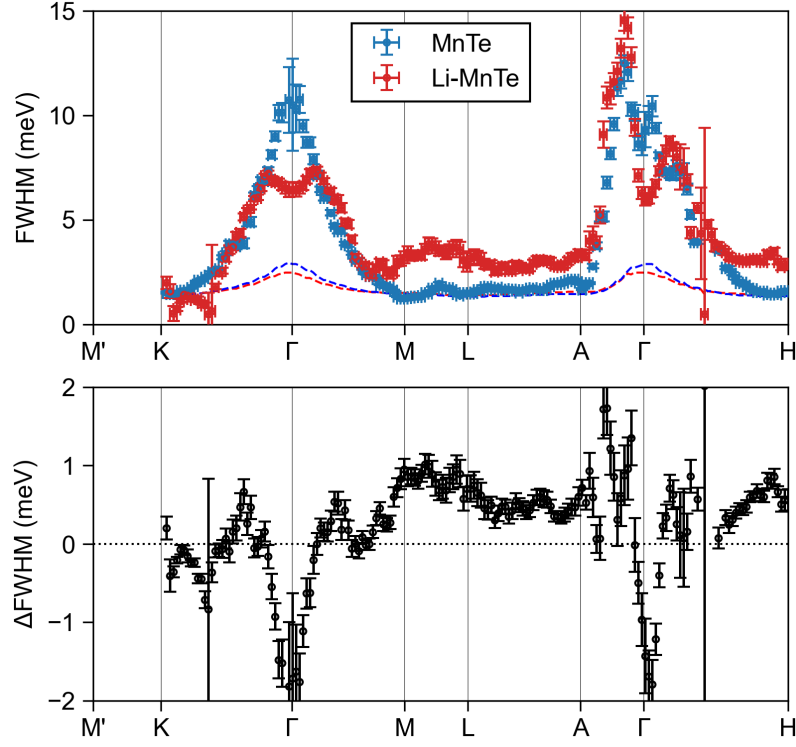
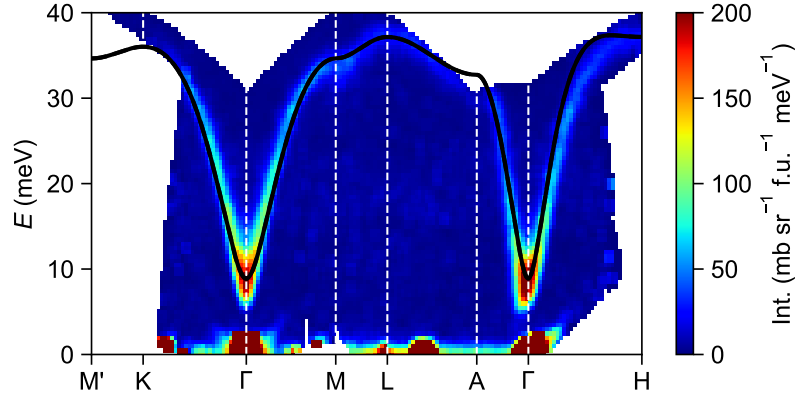
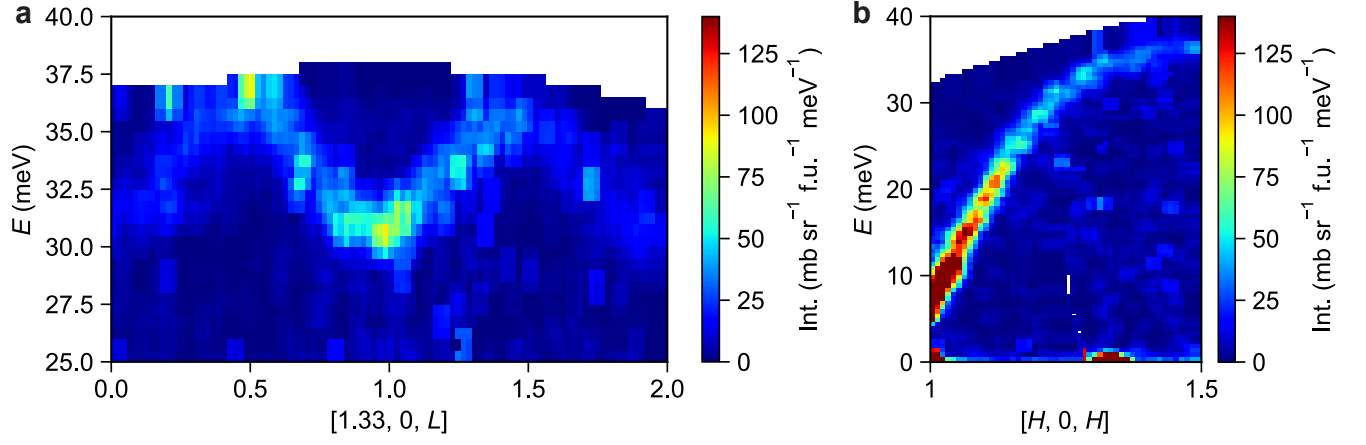
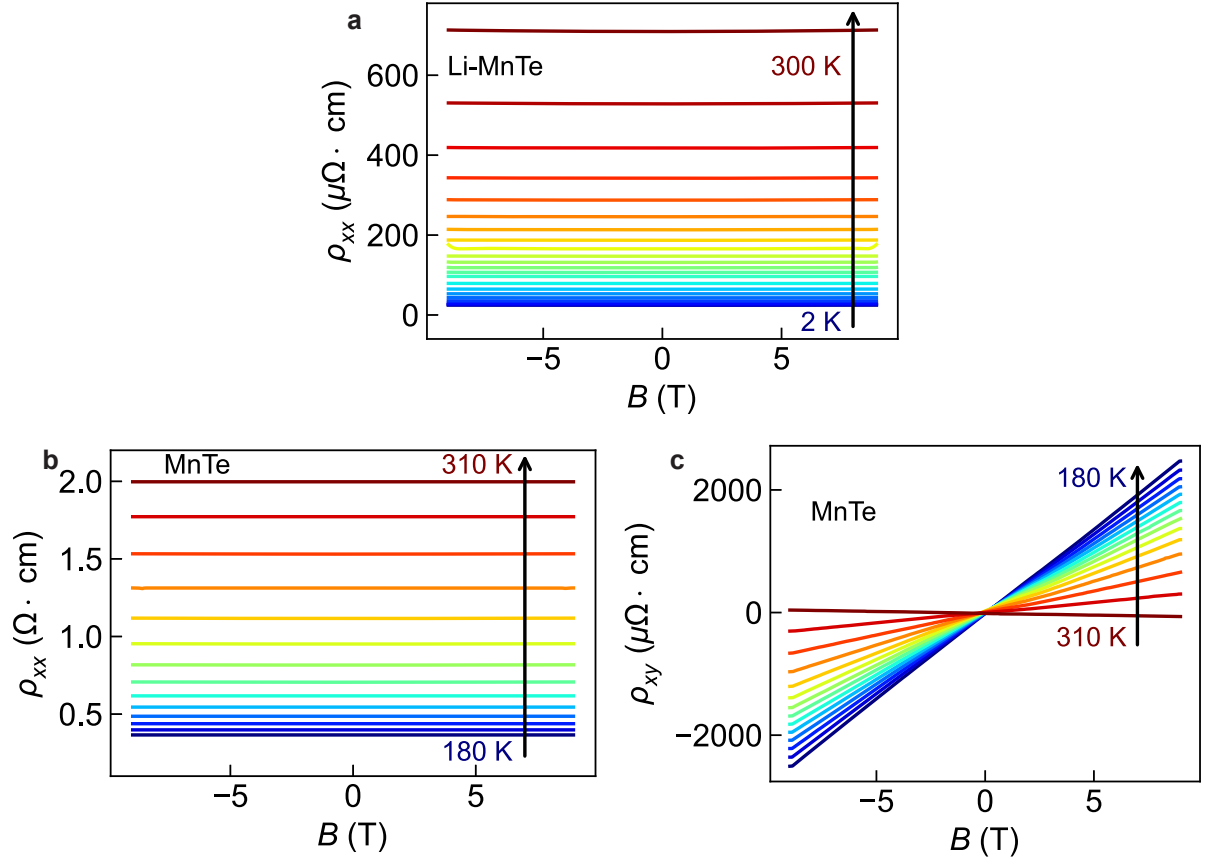


FIG. S2. (Top) Full-width at half-maximum (FWHM) values obtained from Gaussian fits of the spin wave spectra in the nodal planes of the Brillouin zone for undoped α -MnTe and Li-doped α -MnTe. Dashed lines indicate the energy-dependent instrumental resolution from Fig. S1. (Bottom) Δ FWHM values obtained by subtracting the FWHM of undoped α -MnTe from that of Li-doped α -MnTe. Vertical error bars represent 1σ standard deviations and horizontal error bars indicate the q integration range for each line cut.

INS DATA FOR LI-DOPED α -MnTe TAKEN USING THE HR MODEFIG. S3. Spin waves in Li-doped α -MnTe along high-symmetry directions in high-resolution mode.FIG. S4. (a) INS spectra of Li-doped α -MnTe along the $[1.33, 0, L]$ and (b) $[H, 0, H]$ directions in high-resolution mode.

ADDITIONAL TRANSPORT DATA

FIG. S5. Longitudinal and transverse resistivity ρ_{xx} and ρ_{xy} of pure and Li-doped α -MnTe.

LOCAL MOMENT SUM RULE

The total moment sum rule requires $\mathbf{M}_0^2 = \mathbf{M}^2 + \langle \mathbf{m}^2 \rangle = g^2 S(S+1)$, where \mathbf{M} is the static ordered moment contribution (as obtained from the refined magnetic structure using neutron diffraction) and

$$\langle \mathbf{m}^2 \rangle = \frac{3\hbar}{\pi} \int_{-\infty}^{\infty} \frac{\chi''(\omega) d\omega}{1 - \exp(-\hbar\omega/k_B T)}. \quad (2)$$

is the dynamic contribution where $\chi''(\omega)$ is the \mathbf{Q} -averaged local dynamic susceptibility, $E = \hbar\omega$, and k_B is the Boltzmann constant [48]. $\chi''(\mathbf{Q}, \omega)$ is directly related to the measured quantity $S(\mathbf{Q}, E)$ from INS experiments, and can be integrated over a full BZ to yield the energy dependence of the local dynamic susceptibility $\chi''(\omega)$. The \mathbf{Q} -averaged local dynamic susceptibility is given by

$$\chi''(\omega) = \int_{\text{BZ}} \chi''(\mathbf{Q}, \omega) d\mathbf{Q} \quad (3)$$

where the subscript BZ denotes \mathbf{Q} -integration over a full Brillouin zone. The relationship between $\chi''(\mathbf{Q}, \omega)$ and the neutron scattering intensity $I(\mathbf{Q}, E)$ measured during the experiment is given by

$$\chi''(\mathbf{Q}, \omega) = \frac{\pi}{2} \mu_B^2 (1 - e^{-\hbar\omega/k_B T}) \frac{13.77(\text{b}^{-1}) I(\mathbf{Q}, E)}{|f(\mathbf{Q})|^2 e^{-2W}} \quad (4)$$

where $I(\mathbf{Q}, E)$ is assumed to be in absolute units of $\text{b sr}^{-1} \text{ f.u.}^{-1} \text{ meV}^{-1}$, $1 \text{ b} = 10^{-24} \text{ cm}^2$ is the unit “barn” for the neutron scattering cross section, $f(\mathbf{Q})$ is the magnetic form factor, and e^{-2W} is the Debye-Waller factor [43].

\mathbf{Q} -integration of the total spectral weight requires enough coverage to capture a full Brillouin zone, or, at least, enough coverage to reconstruct the full Brillouin zone from a smaller, symmetric portion of it. Because the accessible range of momentum transfer at a given energy transfer is restricted by the kinematic condition, coverage gradually shifts to higher \mathbf{Q} at higher energy transfers. As a result, the coverage at smaller \mathbf{Q} [*e.g.*, $\mathbf{Q} = (1, 0, 1)$] is better at low energies, and the coverage at larger \mathbf{Q} [*e.g.*, $\mathbf{Q} = (1, 0, 3)$] is better at high energies. In order to capture the total spectral weight over the full energy range of the spin waves, $\mathbf{Q} = (1, 0, 1)$ was used for lower energy transfers, and $\mathbf{Q} = (1, 0, 3)$ was used for higher energy transfers, with the specific range informed by the coverage of the respective instrument for MAPS and SEQUOIA datasets.

MOMENTUM- AND ENERGY-INTEGRATION RANGES FOR THE DATA

In the colormaps Fig. 2(a)(b), S2 and S3, the integration and plotting directions are mutually perpendicular. The integration ranges were chosen to ensure that the integrated volume in reciprocal space (in units of \AA^{-1}) is consistent across different directions throughout each figure. Integration ranges for other figures are provided in Table S12. For datasets where altermagnetic splitting is expected, such small integration ranges may be necessary to resolve the splitting clearly.

TABLE S11. Momentum-integration ranges for Fig. 2 (a)-(b), S2 and S3

Plot direction	Integration direction 1	Integration range 1 (r.l.u.)	Integration direction 2	Integration range 2 (r.l.u.)
Γ -M	$[-0.5K, K, 0]$	± 0.0578	$[0, 0, L]$	± 0.093
M-L	$[H, 0, 0]$	± 0.05	$[0, 0, L]$	± 0.093
L-A	$[-0.5K, K, 0]$	± 0.0578	$[0, 0, L]$	± 0.093
Γ -A	$[H, 0, 0]$	± 0.05	$[0, 0, L]$	± 0.093
Γ -H	$[K, -K, 0]$	± 0.05	$[L, L, -6.89L]$	± 0.012
Γ -K-M'	$[K, -K, 0]$	± 0.05	$[0, 0, L]$	± 0.093

TABLE S12. Momentum- and energy-integration ranges for other figures

Data	Momentum 1 (r.l.u.)	Momentum 2 (r.l.u.)	Momentum 3 (r.l.u.)	Energy (meV)
Fig. 2(c)-(e) Fig. 3(h)(i)	$[H, 0, 0], \pm 0.05$	$[-0.5K, K, 0], \pm 0.06$	$[0, 0, L], \pm 0.05$	N/A
Fig. 3(a)(b)	$[H, 0, 0], \pm 0.03$	$[-0.5K, K, 0], \pm 0.02$	N/A	N/A
Fig. 3(c)(d)	$[-0.5K, K, 0], \pm 0.08$	$[L, 0, -3.45L], \pm 0.01$	N/A	N/A
Fig. 3(f)	$[H, 0, 0], \pm 0.02$	$[-0.5K, K, 0], \pm 0.04$	$[0, 0, 0.5L], \pm 0.04$	N/A
Fig. 3(g)	$[0.5H, 0, 0.5H], \pm 0.04$	$[-0.5K, K, 0], \pm 0.04$	$[0.29L, 0, -L], \pm 0.02$	N/A
Fig. 4(a)-(c)	$[0, 0, L], \pm 0.02$	N/A	N/A	± 0.5
Fig. S3(a)	$[H, 0, 0], \pm 0.02$	$[-0.5K, K, 0], \pm 0.04$	N/A	N/A
Fig. S3(b)	$[-0.5K, K, 0], \pm 0.04$	$[L, 0, -3.45L], \pm 0.01$	N/A	N/A